

Online Identification of Inductance and Flux Linkage for Inverter-Fed SPMSMs Using Switching State Functions

Xiaoyan Huang[✉], Member, IEEE, Yelong Yu[✉], Zhaokai Li[✉], Zhuo Chen[✉], Shaopo Huang[✉], Feng Niu[✉], Member, IEEE, and Jian Zhang[✉]

Abstract—This article presents an online method to acquire the stator inductance and flux linkage for inverter-fed surface-mounted permanent magnet synchronous motors (SPMSMs) using switching state functions instead of average models. Given the switching state functions when different voltage vectors are applied to the motors, the information of inductance and flux linkage is revealed. Based on the dc bus voltage and current derivatives obtained from either hardware methods like Rogowski coil and differential circuit, or software methods such as tracking differentiator, stator inductance, and flux linkage are able to be figured out directly using the redundant or more practical methods with the help of recursive least square (RLS). Simulations and experiments are carried out to prove the effectiveness of the proposed methods, besides, dc voltage and operating speed variation as well as the impact of resistance are taken into account. Finally, compared with the conventional parameter identification based on the average models either in α - β or d - q coordinate, the proposed methods with switching state functions have remarkable advantages especially when the rotor position error exists. What needs further effort is the challenging case at very low speed, e.g., it is hard to identify flux linkage due to the small back electromotive force (EMF).

Index Terms—Parameter identification, surface-mounted permanent magnet synchronous motors (SPMSMs), switching state functions.

I. INTRODUCTION

SURFACE-mounted permanent magnet synchronous motors (SPMSMs) have been widely used in most industrial

Manuscript received 24 December 2021; revised 22 March 2022 and 23 July 2022; accepted 8 September 2022. Date of publication 13 September 2022; date of current version 10 October 2022. This work was supported in part by the National Key R&D Program of China under Grant 2019YFE0123500, in part by the Zhejiang Provincial Ten-Thousand-Talents Plan under Grant 2019R52003, and in part by the Liaoning Provincial Natural Science Foundation of China under Grant 2021-KF-24-03. Recommended for publication by Associate Editor J. Hur. (Corresponding authors: Feng Niu; Jian Zhang.)

Xiaoyan Huang, Yelong Yu, Zhaokai Li, Zhuo Chen, and Jian Zhang are with the Zhejiang University, Hangzhou 310058, China (e-mail: xiaoyanhuan@zju.edu.cn; yuelong@zju.edu.cn; lzk_zju@zju.edu.cn; z.chen@zju.edu.cn; jian_zhang_zju@zju.edu.cn).

Shaopo Huang is with the College of Information Engineering, Beijing Institute of Petrochemical Technology, Beijing 102627, China (e-mail: huangshaopo@bjpt.edu.cn).

Feng Niu is with the State Key Laboratory of Reliability and Intelligence of Electrical Equipment, Hebei University of Technology, Tianjin 300401, China (e-mail: niufeng@hebut.edu.cn).

Color versions of one or more figures in this article are available at <https://doi.org/10.1109/TPEL.2022.3206119>.

Digital Object Identifier 10.1109/TPEL.2022.3206119

applications due to their prominent advantages of high torque density and high efficiency [1]. The parameters of inverter-fed SPMSMs are crucial in advancing motor control algorithms [2], [3], particularly for general-purpose motor drivers. In addition, some parameters could be used to monitor the health conditions of SPMSMs, for instance, the value of flux linkage could directly reflect the uniform demagnetization fault [4].

In the literature, many offline and online approaches were developed to improve the accuracy of parameter identification. The standard procedure of measuring the motor parameters by standstill frequency response testing was listed in [5]. Besides, a sine-triangle PWM signal was assigned as input excitation to obtain the offline identification of electrical parameters [6]. As stated in [7], the motor parameters at the standstill could be identified based on integral calculation. Although these offline methods can provide accurate values of motor parameters, they are unable to be applied when SPMSMs are under operation.

In order to detect the parameters when motors are working, quantities of online algorithms were presented to estimate motor parameters [8], [9]. The stator resistance had been identified online to improve the accuracy of position estimation in the sensorless drive system [10]. An adaptive full-state feedback control is proposed to estimate the motor parameters online for the SPMSMs in [11]. Fast and slow parameter estimation algorithms are combined to identify all four electrical parameters in [12] and [13], which reported that the proposed methods in these articles are able to avoid the rank-deficient problem in the steady state [14], [15]. In addition, the signal injection techniques are utilized to deal with the same problem [16], and the harmonics in motor speed are extracted to analyze the magnet flux linkage in [17] and [18]. However, most of the aforementioned online algorithms are implemented in the well-known d - q rotational coordinate using average models, which means these algorithms require precise knowledge of rotor position gained from position sensors such as encoder and resolver. When the resolution of these position sensors related to motor poles is comparatively low, the rotor position errors may exist. In sensorless control systems, it is more difficult to gain the rotor position precisely. Definitely, the rotor position error will terribly influence the accuracy of parameter identification. What is worse, the use of average models will omit the details of PWM switching with different voltage vectors [14], [15].

Recently, more attention is paid on the effect of PWM when estimating motor parameters. Popov et al. [19] proposed an estimation algorithm of motor input impedance using the intrinsic PWM excitation. Similarly, an online stator inductance estimation with PWM excitation is presented in [20]. It was clarified in [21] that full parameters could be estimated even in the steady state by introducing the current ripple model at PWM frequency to current state equations, however, the experimental validation was missing and the impact of dead-band time was not taken into consideration. An extended-Kalman-filter (EKF)-based method was reported in [22] to estimate the motor parameters for synchronous reluctance motors, which may cause a heavy burden on the computational resources. A PWM-based flux linkage estimation method was presented to estimate rotor temperature for PMSMs in [23], the method was still derived from $d-q$ rotational coordinate and the results might deviate from the real values of parameters with the rotor position error. The inductance could be identified successfully through sampling PWM current ripple [24], [25], however, the identifications of other motor parameters such as flux linkage are still missing.

In this article, a way to acquire the inductance and flux linkage for SPMSMs using switching state functions is demonstrated. Based on the dc bus voltage and the first-order current derivatives obtained from either hardware methods like Rogowski coil and differential circuit, or software methods such as tracking differentiator (TD) algorithm after measuring phase current, stator inductance, and flux linkage are able to be figured out directly using the redundant or more practical methods with the help of recursive least square (RLS). Moreover, it is noticed that the items of resistance cannot be neglected in some cases, e.g., when the motor speed is fairly low, thus the solutions with the second-order current derivatives are proposed to estimate the resistance. Simulations and experiments are carried out to prove the effectiveness of proposed methods, besides, dc voltage and operating speed variation as well as the impact of resistance are taken into account. Finally, compared with the conventional parameter identification based on the average models in $d-q$ coordinate, the accuracy of the proposed methods including redundant and practical ones can be still guaranteed even when the rotor position error exists.

II. SPMSM MODEL WITH SWITCHING STATE FUNCTIONS

The widely known average model of SPMSMs in $d-q$ rotational coordinate is stated in the following:

$$u_d = Ri_d + L \frac{di_d}{dt} - \omega_e Li_q, \quad u_q = Ri_q + L \frac{di_q}{dt} + \omega_e Li_d + \omega_e \Psi_f \quad (1)$$

where $u_{d,q}$ and $i_{d,q}$ are the d/q -axis voltages and currents, respectively; R is the stator resistance; L is the stator inductance; ω_e denotes the electrical angular speed; ψ_f refers to the flux linkage. The quantities in $d-q$ coordinate are from the $a-b-c$ coordinate through Park transformation with the precise rotor position angle. When the parameters identification method is executed in $d-q$ coordinate, the rotor position error will significantly affect the results of parameters estimation. In this average

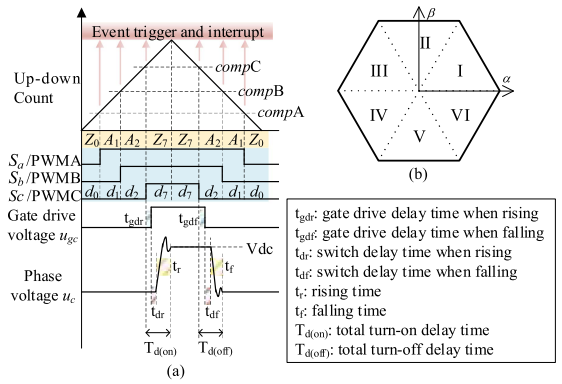


Fig. 1. Waveforms and sectors of SVPWM.

model, quantities such as $u_{d,q}$ and $i_{d,q}$ are always regarded as constant values in steady state. Additionally, the average model in $\alpha-\beta$ coordinate for SPMSMs is written as

$$\begin{aligned} u_\alpha &= Ri_\alpha + L \frac{di_\alpha}{dt} - \omega_e \Psi_f \sin \theta_e, \\ u_\beta &= Ri_\beta + L \frac{di_\beta}{dt} + \omega_e \Psi_f \cos \theta_e \end{aligned} \quad (2)$$

where $u_{\alpha,\beta}$ and $i_{\alpha,\beta}$ are the α/β -axis voltages and currents respectively; θ_e denotes the electrical angle from rotor position sensors. Similarly, in the average model of $\alpha-\beta$ coordinate, the quantities like $u_{\alpha,\beta}$ and $i_{\alpha,\beta}$ are sinusoidal values, and the rotor position is still an important factor to identify the parameters [26]. These average models will always neglect the details and effects of PWM switching for inverter-fed SPMSMs.

Generally, the SPMSMs are driven by the voltage source inverter (VSI) with the space vector pulselwidth modulation (SVPWM). As shown in Fig. 1, the whole space is divided into six sectors, in each sector, the output voltage is combined with two active vectors (A_1, A_2) and two zero vectors (Z_0, Z_7). It is mentioned above the “averaged models” [23] for SPMSMs, either in $d-q$ (1) or $\alpha-\beta$ coordinate (2), always ignore the details in a single PWM period. Actually, the voltage functions in a single PWM period should be separated as several switching states according to the different voltage vectors shown in Fig. 1. For a certain voltage vectors (active or zero), the voltages injected to the motor in $\alpha-\beta$ coordinate could be written as

$$\begin{aligned} u_{\alpha s} &= \frac{2}{3} \left(u_a - \frac{1}{2} u_b - \frac{1}{2} u_c \right) = \frac{1}{3} (u_{ab} + u_{ac}) \\ &= \frac{\text{Vdc}}{3} (2S_a - S_b - S_c) \\ u_{\beta s} &= \frac{2}{3} \left(\frac{\sqrt{3}}{2} u_b - \frac{\sqrt{3}}{2} u_c \right) = \frac{\sqrt{3}}{3} u_{bc} = \frac{\sqrt{3}\text{Vdc}}{3} (S_b - S_c) \end{aligned} \quad (3)$$

where $u_{\alpha s, \beta s}$ are the α/β -axis voltages in switching state functions; $u_{a,b,c}$, $u_{ab,ac,bc}$ are the phase or line-to-line voltages in $a-b-c$ coordinate; Vdc is the dc bus voltage; $S_{a,b,c}$ denote the switching state of devices, $S = 1$ means the high-side switch device is on while $S = 0$ means the low-side one is on. According

TABLE I
VOLTAGE VECTORS IN DIFFERENT SECTORS

Sector	Vector	S_a	S_b	S_c	$u_{\alpha s}$	$u_{\beta s}$
I	A_1	1	0	0	2/3Vdc	0
	A_2	1	1	0	1/3Vdc	$\sqrt{3}/3$ Vdc
II	A_1	0	1	0	-1/3Vdc	$\sqrt{3}/3$ Vdc
	A_2	1	1	0	1/3Vdc	$\sqrt{3}/3$ Vdc
III	A_1	0	1	0	-1/3Vdc	$\sqrt{3}/3$ Vdc
	A_2	0	1	1	-2/3Vdc	0
IV	A_1	0	0	1	-1/3Vdc	$-\sqrt{3}/3$ Vdc
	A_2	0	1	1	-2/3Vdc	0
V	A_1	0	0	1	-1/3Vdc	$-\sqrt{3}/3$ Vdc
	A_2	1	0	1	1/3Vdc	$-\sqrt{3}/3$ Vdc
VI	A_1	1	0	0	2/3Vdc	0
	A_2	1	0	1	1/3Vdc	$-\sqrt{3}/3$ Vdc
zero vector	Z_0	0	0	0	0	0
	Z_7	1	1	1	0	0

to (3), the values of $u_{\alpha s}, u_{\beta s}$ with different active and zero vectors in all six sectors are listed in Table I.

The switching state's monitoring of devices is of great importance in the next parameters identification procedure, hence some methods that can be implemented in experiments for such monitoring are illustrated beforehand. (i) A very simple method is to use the voltage sensors to directly measure the line-to-line voltages from the motor terminals, with which the values of $u_{\alpha s}$ and $u_{\beta s}$ can be calculated according to (3). (ii) Besides, the PWM signals can be connected to GPIOs of DSP/MCU and the switching state can be also known by reading GPIOs, which does not require additional sensors but the total turn-on/turn-off delay time presented in Fig. 1 must be taken into account. (iii) Another practical approach enabling to be implemented in DSP/MCU is event and interrupt trigger when the up-down count reaches up to the compared values of three phases [27], which makes the DSP/MCU know the state of switching devices. Note that this approach is only available when the algorithms of motor control and parameter estimation are executed in the same DSP/MCU. Similarly, the total turn-ON/turn-OFF delay time should be taken into account and, during these periods the sampling procedure should be disabled. In this article, method (i) is used when the TD algorithm is applied as shown in Fig. 4; while method (iii) is utilized when current derivatives are measured with Rogowski coil and differential circuit for its convenience.

With the values of $u_{\alpha s}$ and $u_{\beta s}$ in Table I, the switching state functions in α - β coordinate are given as

$$\begin{aligned} \frac{di_{\alpha s}}{dt} &= \left[\frac{u_{\alpha s}}{L} \right] + \left(-\frac{R}{L} i_{\alpha s} + \frac{\omega_e \Psi_f}{L} \sin \theta_e \right) \\ \frac{di_{\beta s}}{dt} &= \left[\frac{u_{\beta s}}{L} \right] + \left(-\frac{R}{L} i_{\beta s} - \frac{\omega_e \Psi_f}{L} \cos \theta_e \right) \end{aligned} \quad (4)$$

constant part + sinusoid part

where $i_{\alpha s}, i_{\beta s}$ are the α/β -axis currents in switching state functions. Some issues should be clarified about the switching state functions (4). First, there are only several specific and constant values for $u_{\alpha s}$ and $u_{\beta s}$, $u_{\alpha s}$ is always equal to -2/3, -1/3, 0, 1/3, 2/3 Vdc while $u_{\beta s}$ is always equal to $-\sqrt{3}/3$ Vdc, 0, $\sqrt{3}/3$ Vdc,

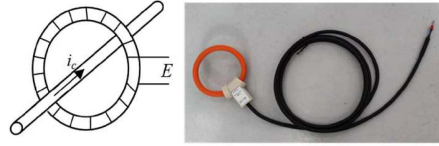


Fig. 2. Basic structure of Rogowski coil and its picture.

which could be clearly seen from Table I. Second, the items of flux linkage must be the same as average model in (2). Third, the values of $i_{\alpha s}$ and $i_{\beta s}$ can also be regarded equal to their average values, namely, i_α and i_β in (2), which is based on the assumption of ignoring the current ripples caused by PWM switching. It should be noted that the current ripples could be neglected for the values of $i_{\alpha s}$ and $i_{\beta s}$, while is unable to be ignored when figuring out the values of $di_{\alpha s}/dt$ and $di_{\beta s}/dt$. In fact, the active time of voltage vectors within one PWM period shown in Fig. 1 is fairly small, always in the level of microsecond, which results in the large values of $di_{\alpha s}/dt$ and $di_{\beta s}/dt$ instead of the average values di_α/dt and di_β/dt . Hence, the value of $di_{\alpha s}/dt$ and $di_{\beta s}/dt$ in the switching state functions should be accurately measured, either through sensors or calculating the differential of measured currents. It has been mentioned above that the quantities of the average model in (2) could be regarded as sinusoid values, thus, the current derivatives $di_{\alpha s}/dt$ and $di_{\beta s}/dt$ in (4) could be divided into two independent parts, namely, constant and sinusoid parts. In the sinusoid parts, the items of R could be neglected in high/middle speeds, while the impact of R at low speed will be discussed later, in Section IV-D. Finally, although θ_e still appears in (4), further study can manifest that the value of θ_e in switching state functions will have no impact on the identification of inductance and flux linkage.

III. CURRENT DERIVATIVE MEASUREMENT

Since the current derivatives are used to identify the parameters in this article, the alternative method either by hardware or software to obtain the current derivatives are first illustrated in this section, in addition, the pros and cons of these methods are also stated.

A. Current Derivative Measurement With Rogowski Coil

Some sensors for exclusive use of current derivative measurement like Rogowski coil can be used to detect the current derivatives. The basic structure of the Rogowski coil and its picture are shown in Fig. 2, the induced voltage in the Rogowski coil wound around the crossing conductors reflect the change of conductor current [29], which can be written as

$$E = M di_c/dt \quad (5)$$

where M is the transform coefficient between the derivative of conductor current i_c and induced voltage E in the Rogowski coil.

The Rogowski coil could be used in the high-power applications to measure the derivative of large currents, and it does not require other current sensors like Hall sensors to measure current derivative. However, the additional cost of Rogowski

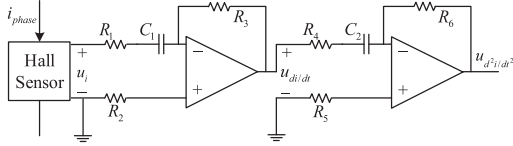


Fig. 3. Differential circuit.

coil is always high, and it is hard to be installed on the PCB and integrated in the inverter systems.

B. Current Derivative Measurement With Differential Circuit

Another approach to measure the current derivative is using differential operational circuit. As shown in Fig. 3, the differential circuit is attached to the end of phase current sampling with Hall current sensors. It can be simply calculated

$$u_{di/dt} = -R_3 C_1 \frac{du_i}{dt}, \quad u_{d^2i/dt^2} = -R_6 C_2 \frac{du_{di/dt}}{dt}. \quad (6)$$

R_1 and R_4 are very small and important resistors ($R_1 \ll R_3$, $R_4 \ll R_6$) for limiting the input currents when the input voltages change sharply, which enables the amplifiers to work in amplification region. The second-order current derivative is used to estimate resistance in some cases that will be stated next.

It is believed that the cost of an operational amplifier could be much lower than the Rogowski coil, which could be accepted in most cases. Moreover, it is convenient to embed the differential circuit in the inverter system. But the environment noises and electro-magnetic interference (EMI) should be carefully addressed when designing such a differential circuit. For one thing, the values of C_1 and C_2 should be small relatively (the level of pF in this article) to reduce the noise, since the capacitors are the main differential components in the circuit. For another, the RLS as stated in the following sections is applied to decrease the impact of noise due to its statistical unbiasedness [28].

C. Current Derivative Calculation With Tracking Differentiator

Apart from the direct measurement with hardware methods, the current derivative could be calculated with the software algorithms, in the digital systems, the slope of current $i_{\alpha s}$ can be figured out by the simple differential operation

$$\frac{di_{\alpha s}}{dt} = \frac{i_{\alpha s}(k+1) - i_{\alpha s}(k)}{T_s} \quad (7)$$

where k denotes the k th sample point, T_s is the sample time. However, this simple differential operation will terribly introduce high-frequency noises into the current derivative. The current can be expressed as the following form considering the noises in real world:

$$\tilde{i}_{\alpha s}(k) = i_{\alpha s}(k) + n(k), \quad \tilde{i}_{\alpha s}(k+1) = i_{\alpha s}(k+1) + n(k+1). \quad (8)$$

Assuming that the noises $n(k)$ and $n(k+1)$ in the currents follow the Gaussian distribution with the mean value of zero

$$n(k) \sim N(\mu_0 = 0, \sigma_0^2), \quad n(k+1) \sim N(\mu_1 = 0, \sigma_1^2) \quad (9)$$

where $\mu_{0,1}$, $\sigma_{0,1}$ are the mean values and variances of $n(k)$ and $n(k+1)$, respectively. Then the current derivative considering the noises is written as

$$\begin{aligned} \frac{d\tilde{i}_{\alpha s}}{dt} &= \frac{\tilde{i}_{\alpha s}(k+1) - \tilde{i}_{\alpha s}(k)}{T_s} \\ &= \frac{[i_{\alpha s}(k+1) - i_{\alpha s}(k)] + [n(k+1) - n(k)]}{T_s}. \end{aligned} \quad (10)$$

The noises in k th and $(k+1)$ th point are regarded as independent events, $n(k+1)-n(k)$ also follows the Gaussian distribution:

$$\Delta n(k+1) = [n(k+1) - n(k)] \sim N(\mu_1 - \mu_0 = 0, \sigma_1^2 + \sigma_0^2). \quad (11)$$

Since the current sample time is often small, the noise $\Delta n(k+1)$ has been amplified with the coefficient $1/T_s$. In order to reduce the magnification of noise, the derivative calculation time T_d has to be extended. Equation (10) refers to the situation when $T_d = T_s$, if $T_d = mT_s$ ($m > 1$), it will become

$$\begin{aligned} \frac{d\tilde{i}_{\alpha s}}{dt} &= \frac{\tilde{i}_{\alpha s}(k+m) - \tilde{i}_{\alpha s}(k)}{mT_s} \\ &= \frac{[i_{\alpha s}(k+m) - i_{\alpha s}(k)] + [n(k+m) - n(k)]}{mT_s} \end{aligned} \quad (12)$$

$n(k+m)-n(k)$ still follows the Gaussian distribution:

$$[n(k+m) - n(k)] \sim N(\mu_m - \mu_1 = 0, \sigma_m^2 + \sigma_1^2) \quad (13)$$

where μ_m , σ_m are the mean value and variance of $n(k+m)$, respectively. It can be seen the noise in (12) has been reduced by $1/m$, however, the phase of current derivative will also be changed with the increase of m . Things may become worse with the current derivatives within a small period of PWM, since the sample points is not very adequate for the derivative calculation.

To deal with the noises of current derivative calculation, the famous TD was proposed [30], [31]. In this article, a linear TD is used to calculate current derivatives, which is formed as

$$\begin{aligned} x_1(k+1) &= x_1(k) + T_s x_2(k) \\ x_2(k+1) &= x_2(k) - T_s \left[\frac{x_1(k) - \tilde{i}_{\alpha s}(k)}{T_d^2} + \frac{2x_2(k)}{T_d} \right] \end{aligned} \quad (14)$$

where x_1 is the desired trajectory of current $i_{\alpha s}$ and x_2 is its derivative. Substituting $\tilde{i}_{\alpha s}(k)$ in (14) with the items in (8) yields

$$\begin{aligned} x_2(k+1) &= x_2(k) - T_s \left[\frac{x_1(k) - i_{\alpha s}(k)}{T_d^2} + \frac{2x_2(k)}{T_d} \right] \\ &\quad + \frac{T_s}{T_d^2} n(k). \end{aligned} \quad (15)$$

It can be obviously seen that the noise can be reduced by $1/m^2$ when $T_d = mT_s$, which means the TD has better performance on the noise suppression than the simple differential operation in (12).

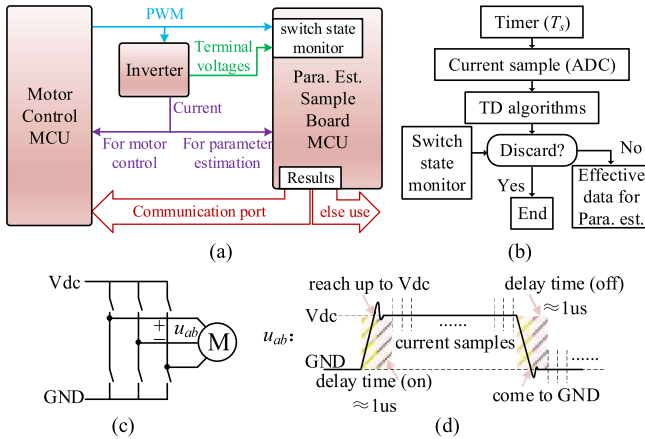


Fig. 4. Hardware and software implementation when TD is applied. (a) hardware. (b) software implementation. (c) voltage-source inverter. (d) judging mechanism.

TABLE II
PROS AND CONS OF METHODS FOR CURRENT DERIVATIVE MEASUREMENT

Method	Rogowski Coil	Differential circuit	TD
Advantages	derivative measuring of large currents	low cost and be embedded easily	no need for other hardware
Disadvantages	high cost and hard for integration.	noises and EMI should be addressed	high-rate ADCs and extra computation

Although the current derivative can be calculated through software method, it still requires high-rate analog-to-digital conversions (ADCs), which means the additional cost may be transferred to DSP/MCU. In this article, the sample time T_s when TD is applied is set as $2 \mu s$ (not switching period), with such a high-frequency sampling, another independent DSP/MCU is needed in the experiments for parameters estimation as shown in Fig. 4. The currents are measured for both motor current loop control and parameter estimation. In the software execution, the TD algorithms can be implemented after the current sampling. Monitoring the switching state of devices by the approaches stated in Section II, a judging mechanism is designed to discard the data during the transient switching process. As stated previously, the terminal voltages are directly used to monitor the switching states (method i) when TD is applied shown in Fig. 4(c), the transient switching process can be easily discarded when the measured terminal voltages reach up to Vdc or come to GND with a delay time ($\approx 1\mu s$) shown in Fig. 4(d). Other effective data can be used for the parameter estimation.

Finally, the pros and cons of above methods to measure or calculate current derivatives are summarized in Table II.

IV. METHOD OF IDENTIFYING STATOR INDUCTANCE AND FLUX LINKAGE

After getting the current derivatives using the methods in Section III, the stator inductance and flux linkage are able to be identified, which will be illustrated in this section.

A. Inductance and Flux Linkage Identification

It can be known from (4) that the constant part of current derivatives contains the crucial information of stator inductance L . As mentioned before and listed in Table I, $u_{\alpha s}$ and $u_{\beta s}$ are within several explicit values related to Vdc, which makes it easy to obtain $u_{\alpha s}$ and $u_{\beta s}$ in different vectors by measuring the dc bus voltage. Then the value of inductance L is able to be figured out after extracting the constant parts of current derivatives $di_{\alpha s}/dt$ and $di_{\beta s}/dt$.

For most SPMSMs, the stator resistance is designed as small value to reduce the copper loss, which means the items of R can be ignored for its small proportion in the sinusoid part compared with the items of $\omega_e \psi_f$, especially for the high-speed motors (the impact of resistance at low speed or large current are stated in Section IV-D). With this assumption, the amplitudes of sinusoid parts in (4) reflect the value of flux linkage ψ_f when the inductance L can be calculated beforehand through the constant part.

B. Redundant Methodology for Extraction of Constant and Sinusoid Parts in Current Derivatives

Current derivatives can be written as the addition of constant part and sinusoid part (sinusoid part could be expressed as two orthogonal components), e.g., in α -axis, it is

$$\frac{di_{\alpha s}}{dt} = A_{\alpha} + B_{\alpha} \sin \theta_e + C_{\alpha} \cos \theta_e \quad (16)$$

where $A_{\alpha, \beta}$, $B_{\alpha, \beta}$, and $C_{\alpha, \beta}$ are the coefficients awaiting to be identified.

By using the algorithm of RLS, the coefficients above can be estimated, the iteration process of coefficients update is described as follows, let:

$$y = \hat{\mathbf{W}}^T \mathbf{X} \quad (17)$$

$$\text{where : } y = \frac{di_{\alpha s}}{dt}, \quad \mathbf{X} = [1 \quad \sin \theta_e \quad \cos \theta_e]^T,$$

$$\hat{\mathbf{W}} = [A_{\alpha} \quad B_{\alpha} \quad C_{\alpha}]^T. \quad (18)$$

Then the general RLS algorithm is derived as [13]

$$\begin{aligned} \hat{\mathbf{W}}(i) &= \hat{\mathbf{W}}(i-1) + \mathbf{K}(i) [y(i) - \hat{\mathbf{W}}(i-1)^T \mathbf{X}(i)] \\ \mathbf{K}(i) &= \frac{\mathbf{P}(i-1) \mathbf{X}(i)}{\lambda + \mathbf{X}(i)^T \mathbf{P}(i-1) \mathbf{X}(i)} \\ \mathbf{P}(i) &= [\mathbf{I} - \mathbf{K}(i) \mathbf{X}(i)^T] \times \mathbf{P}(i-1) / \lambda \end{aligned} \quad (19)$$

where i is the iteration number; \mathbf{K} , \mathbf{P} are the supplementary variables; \mathbf{I} is the identity matrix; λ is the forgetting factor to avoid the data saturation. It should be also noted that some conditions must be satisfied when applying the RLS algorithm like: 1) adequate data are required to avoid the rank deficiency problems, at least three samples to identify the three unknown parameters A_{α} , B_{α} , and C_{α} ; (ii) try to select the samples from different positions (not concentrated) of sinusoid curve to prevent ill convergence. According to listed values of $u_{\alpha s}$ in Table I, the samples when $u_{\alpha s} = \pm 2/3Vdc$ would be better abandoned since

they have the least number of data and are very concentrated, which may cause bad convergent results.

The α -axis function in (16) will be divided into five RLS algorithms according to different values of $u_{\alpha s}$ listed in Table I, while the β -axis function has three RLS algorithms. Take the α -axis function as an example, it can be expressed as

$$di_{\alpha s}/dt = A_{\alpha 1} + B_{\alpha 1} \sin \theta_e + C_{\alpha 1} \cos \theta_e \quad (u_{\alpha s} = -2/3Vdc) \quad (20)$$

$$di_{\alpha s}/dt = A_{\alpha 2} + B_{\alpha 2} \sin \theta_e + C_{\alpha 2} \cos \theta_e \quad (u_{\alpha s} = -1/3Vdc) \quad (21)$$

$$di_{\alpha s}/dt = A_{\alpha 3} + B_{\alpha 3} \sin \theta_e + C_{\alpha 3} \cos \theta_e \quad (u_{\alpha s} = 0) \quad (22)$$

$$di_{\alpha s}/dt = A_{\alpha 4} + B_{\alpha 4} \sin \theta_e + C_{\alpha 4} \cos \theta_e \quad (u_{\alpha s} = 1/3Vdc) \quad (23)$$

$$di_{\alpha s}/dt = A_{\alpha 5} + B_{\alpha 5} \sin \theta_e + C_{\alpha 5} \cos \theta_e \quad (u_{\alpha s} = 2/3Vdc) \quad (24)$$

Comparing (4) and (20)–(24), the values of inductance and flux linkage can be identified as

$$L = \frac{-2/3Vdc}{A_{\alpha 1}} = \frac{-1/3Vdc}{A_{\alpha 2}} = \frac{1/3Vdc}{A_{\alpha 4}} = \frac{2/3Vdc}{A_{\alpha 5}}. \quad (25)$$

Ignoring the impact of resistance, flux linkage is written as

$$\Psi_f = \sqrt{B_{\alpha j}^2 + C_{\alpha j}^2} \times L/\omega_e \quad (j = 1, 2, 3, 4, 5). \quad (26)$$

It can be seen from (26) that the identification of flux linkage is only concerned with the amplitude values of sinusoid part, while has nothing to do with the rotor position angle, which means the rotor position errors have no impact on the identification results.

However, this methodology requires, as much as possible, the data of current derivatives in each voltage vectors, which means the proposed methodology is very redundant and unnecessary data in one PWM period might be also included.

C. Practical Approach for Parameter Identification

As a matter of fact, there is no need to detect current derivatives at each voltage vector and a more practical method is presented here, with which only one active vector and one zero vector are needed to identify parameters in a single PWM period. Take the α -axis function as an example

$$\text{Active vector : } \frac{di_{\alpha s_active}}{dt} = \frac{u_{\alpha s_active}}{L} + \left(-\frac{R}{L} i_{\alpha s} + \frac{\omega_e \Psi_f}{L} \sin \theta_e \right) \quad (27)$$

$$\text{Zero vector : } \frac{di_{\alpha s_zero}}{dt} = 0 + \left(-\frac{R}{L} i_{\alpha s} + \frac{\omega_e \Psi_f}{L} \sin \theta_e \right). \quad (28)$$

Assuming that in one PWM period, the currents, electrical angle and angular speed are regarded as the same, which also

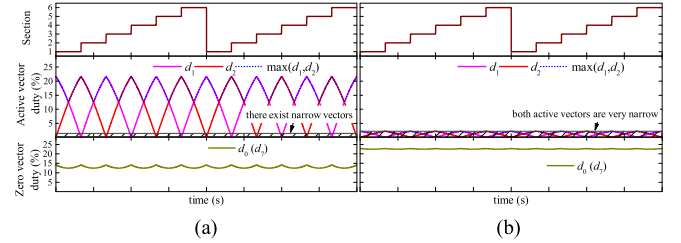


Fig. 5. Duty cycle waveforms of voltage vectors. (a) normal situations. (b) low speed and slight load.

means the sinusoid part is maintained the same, thus

$$L = u_{\alpha s_active} / \left(\frac{di_{\alpha s_active}}{dt} - \frac{di_{\alpha s_zero}}{dt} \right). \quad (29)$$

In terms of identifying ψ_f , the RLS algorithms similar to (16)–(19) can also be applied instead of direct calculation with (28) in order to avoid the impact of rotor position error, let

$$y_p = \hat{\mathbf{W}}_p^T \mathbf{X}_p \quad (30)$$

$$\text{where } y_p = \frac{di_{\alpha s_zero}}{dt}, \mathbf{X}_p = [\sin \theta_e \quad \cos \theta_e]^T,$$

$$\hat{\mathbf{W}}_p = [D_\alpha \quad E_\alpha]^T. \quad (31)$$

Implementing the RLS algorithm similar to (19), ψ_f is gained

$$\Psi_f = \sqrt{D_\alpha^2 + E_\alpha^2} \times L/\omega_e. \quad (32)$$

It should be clarified that L is identified with (29) beforehand and could not be affected by the value of ψ_f . In this practical way, one active and one zero voltage vectors are enough for the parameters estimation and, the accuracy of estimated results can be still guaranteed ignoring those narrow voltage vectors. According to the duty cycle definitions (d_0, d_1, d_2, d_7) for voltage vectors in Fig. 1, in order to get more space for current derivatives measuring, the active vectors with a larger duty cycle which can be expressed as $\max(d_1, d_2)$ in Fig. 5(a) are selected in most normal situations.

However, things may become challenging in some cases, e.g., the voltage is very small at low speed and with a very slight load, which means the space of both two active vectors is very narrow and it is hard to measure the current derivatives, the duty cycle waveforms of both active and zero vectors are presented in Fig. 5(b). It is seen the space of zero vectors is still enough for the current derivative measurement. In order to deal with the problems of narrow active vectors, the technique of PWM shift can be applied, which is widely used in other literatures [32], [33] regarding single-shunt current sensing in motor control.

Another challenging case is over modulation when the required reference voltage is large. The modulation index is usually defined as the ratio of modulated fundamental voltage V_1 and the fundamental voltage at six-step operation [34], [35], [36]

$$m = V_1 / \left(2/\pi Vdc \right). \quad (33)$$

The PWM waveforms when reference voltages locate on the boundary of linear and over modulation ($m = 0.907$) are shown

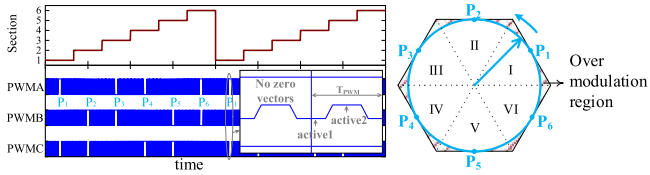


Fig. 6. PWM waveforms when reference voltages locate on the boundary of linear and over modulation, $m = 0.907$.

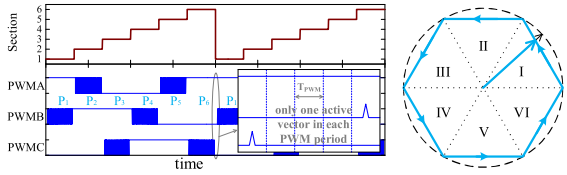


Fig. 7. PWM waveforms when reference voltages locate on the trajectory of SVPWM hexagon, $m = 0.952$.

in Fig. 6, it can be seen that in some points (P₁-P₆), the zero voltage vectors might disappear and only two active vectors are contained in one PWM period T_{PWM}, which means the method described in (27) and (28) may not be available. To deal with that, the methods can be modified using these two active vectors

$$\text{Active vector 1 : } \frac{di_{\alpha s_active1}}{dt} = \frac{u_{\alpha s_active1}}{L} + \left(-\frac{R}{L} i_{\alpha s} + \frac{\omega_e \Psi_f}{L} \sin \theta_e \right) \quad (34)$$

$$\text{Active vector 2 : } \frac{di_{\alpha s_active2}}{dt} = \frac{u_{\alpha s_active2}}{L} + \left(-\frac{R}{L} i_{\alpha s} + \frac{\omega_e \Psi_f}{L} \sin \theta_e \right). \quad (35)$$

Again, the sinusoid parts in the two active vectors of one PWM period can be regarded as the same, then the inductance can be figured out by (if resistance item is ignored)

$$L = (u_{\alpha s_active2} - u_{\alpha s_active1}) / \left(\frac{di_{\alpha s_active2}}{dt} - \frac{di_{\alpha s_active1}}{dt} \right). \quad (36)$$

The value of ψ_f can also be calculated by RLS algorithms, but (31) should be changed to

$$y'_p = \frac{di_{\alpha s_active1}}{dt} - \frac{u_{\alpha s_active1}}{L}, \mathbf{X}_p' = [\sin \theta_e \cos \theta_e]^T, \hat{\mathbf{W}}_p' = [D_\alpha E_\alpha]^T. \quad (37)$$

It will be much more difficult if the reference voltage is continuing to increase until the trajectory fully coinciding with hexagon ($m = 0.952$), shown in Fig. 7. It can be found that there might be only one active voltage vector in each PWM period, with which there is inaccessible way to identify the parameters. The end of this extreme circumstance is so-called “six-step”

TABLE III
PERFORMANCE AND SOLUTION IN DIFFERENT CASES

Cases	Small voltage, e.g., low speed and slight load	Normal situations	Large voltage and over modulation may occur
Perform	Wide zero vectors, narrow active vectors	Enough space for estimating parameters	Zero vectors may disappear and possibly only one active vector in each PWM period
Solution	PWM shift	No need for additional solutions	0.907 < m < 0.952: two active vectors can be used 0.952 < m < 1: still challenging

mode when the modulation index is approaching to 1. Finally, the performance of proposed practical approach and implemented solutions in different cases are summarized in Table III. It is mentioned that the practical approach only need two different voltage vectors in a single PWM, but may fail when only one voltage vector is contained.

D. Impact of Resistance at Low Speed

It is noticed that the proposed method above is based on the assumption of ignoring the resistance, which may not be valid at low speed or the current is significantly large. In other words, the items of resistance occupy a similar or prominent position in the sinusoid part compared to the items of flux linkage. However, $i_d = 0$ control is often adopted for SPMSMs, resulting in that the current and back electromotive force (EMF) are in-phase, thus, the values of R and ψ_f cannot be identified simultaneously from the extracted sinusoid part in (4) due to the ill convergence problems, as pointed out by other literatures [9], [14], [15], [26]. Fortunately, it is possible to identify R and ψ_f simultaneously in steady state for SPMSMs with the switching state functions, which is provided below. The second-order current derivative from (4) in α -axis is given as

$$\frac{d^2 i_{\alpha s}}{dt^2} = \frac{1}{L} \frac{du_{\alpha s}}{dt} - \frac{R}{L} \frac{di_{\alpha s}}{dt} + \frac{\omega_e^2 \Psi_f}{L} \cos \theta_e. \quad (38)$$

Let us see the value of $du_{\alpha s}/dt$, as illustrated previously, $u_{\alpha s}$ is always equal to several constant values related to Vdc, which is listed in Table I. Although $u_{\alpha s}$ is not always equal to a single value, the derivative of $u_{\alpha s}$ during one specific voltage vector can be regarded as zero (Vdc variation will be discussed later). The transient switching process may only lead to a spike on $du_{\alpha s}/dt$. Substituting the α -axis function of (4) into (38), yields

$$\begin{aligned} \frac{d^2 i_{\alpha s}}{dt^2} = & -\frac{R}{L} \left(\frac{u_{\alpha s}}{L} - \frac{R}{L} i_{\alpha s} + \frac{\omega_e \Psi_f}{L} \sin \theta_e \right) + \frac{\omega_e^2 \Psi_f}{L} \cos \theta_e \\ = & \boxed{-\frac{Ru_{\alpha s}}{L^2}} + \boxed{\frac{R^2 i_{\alpha s}}{L^2} + \frac{\omega_e \Psi_f}{L} (\omega_e \cos \theta_e - \frac{R}{L} \sin \theta_e)}. \end{aligned} \quad (39)$$

constant + sinusoid

It can be observed that similar to the first-order current derivative, the second-order current derivative also contains constant and sinusoid parts. The value of R can be identified by extracting the constant part in the second-order current derivative with L , which can be estimated beforehand using the first-order current derivative. After getting value of R , ψ_f can be finally identified by subtracting the items of R from the sinusoid part of (4).

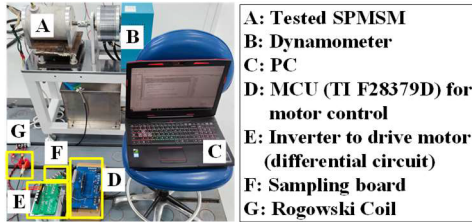


Fig. 8. Experiment setup.

TABLE IV
PARAMETERS OF THE TESTED SPMSM AND INVERTER (20°C)

R	L	Flux linkage	Rated speed	Rated current	Max current	Vdc	Switch frequency
0.08Ω	0.42mH	0.04Wb	6000rpm	10A	30A	150V	4kHz

TABLE V
PARAMETERS IN DIFFERENTIAL CIRCUIT (SEE FIG. 3)

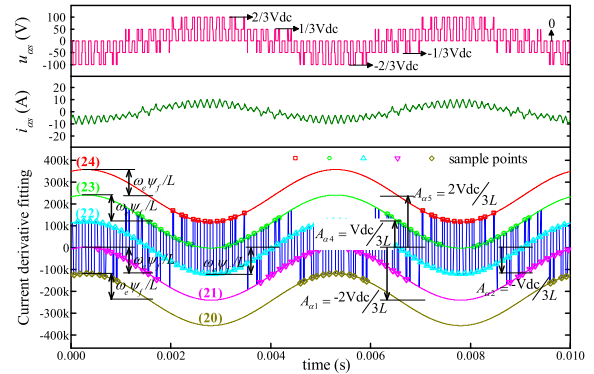
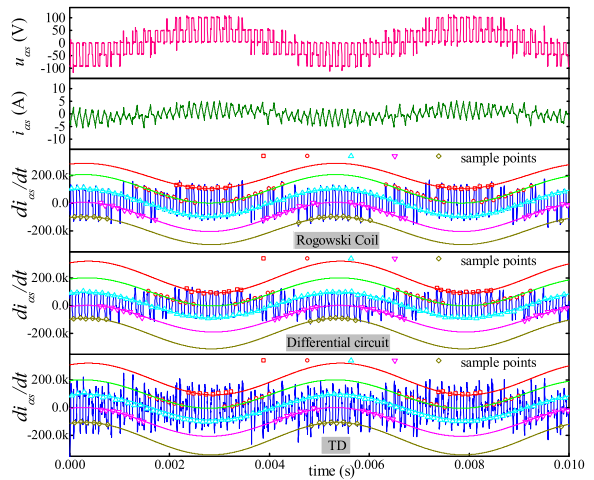
R_1	R_2	R_3	R_4	R_5	R_6	C_1	C_2
100Ω	$1\text{k}\Omega$	$100\text{k}\Omega$	100Ω	$1\text{k}\Omega$	$402\text{k}\Omega$	47pF	47pF

V. SIMULATIONS AND EXPERIMENTS

In this section, simulations based on MATLAB/Simulink and experiments on the test rig are carried out to verify the effectiveness of the proposed method. The experiment setup is photographed in Fig. 8, including the tested SPMSM (36 slots, 4 poles) and the two-level inverter; their parameters are listed in Table IV. The rated motor parameters are from specifications of tested SPMSM and verified by finite-element analysis (FEA) simulation tools. In order to gain the current derivatives through different ways, a board for high-frequency current sampling is equipped in the system when TD algorithm is applied to calculate current derivative as depicted in Fig. 4. In addition, Rogowski coil is also wound around the motor wires and the differential circuit is embedded in the inverter board, parameters of differential circuit (see Fig. 3) are listed in Table V.

A. Rated Conditions

First, the SPMSM is controlled with field-oriented control (FOC) algorithms at its rated conditions, namely, 6000 r/min , the simulated and experimental waveforms of α -axis voltages, currents and current derivatives are shown in Figs. 9 and 10 correspondingly. Note that the proposed methods can also be implemented with β -axis functions, which will not be repeated in this section. In Fig. 9, it can be clearly seen that the voltage $u_{\alpha s}$ have five different values related to Vdc , which is also listed in Table I. Implementing the redundant methodology for extraction of constant and sinusoid parts in current derivatives mentioned in Section IV-B, the fitting results using RLS are also shown in Fig. 9, which is described as (20)–(24). All of the five fitting curves are sinusoids, their amplitudes and offsets ($\sqrt{B_{\alpha j}^2 + C_{\alpha j}^2}$ and $A_{\alpha j}$ in (20)–(26), respectively) contain the information of motor parameters, hence, the values of L and

Fig. 9. Simulated waveforms of $u_{\alpha s}$, $i_{\alpha s}$ and $di_{\alpha s}/dt$ fitting results with RLS.Fig. 10. Experimental waveforms of $u_{\alpha s}$, $i_{\alpha s}$ and $di_{\alpha s}/dt$ fitting results with RLS using Rogowski coil, differential circuit and TD (20°C).

ψ_f can be identified through (25) and (26). In the experiments, all of the methods to gain the current derivative mentioned in Section III are conducted, including Rogowski coil, differential circuit, and TD. When TD is used to calculate current derivative, the sample period T_s and T_d are set as

$$T_s = 2\ \mu\text{s}, \quad T_d = mT_s = 2T_s. \quad (40)$$

Simulated and experimental results of L and ψ_f identifications using α -axis switching state function are listed in Table VI, it is validated that estimated L and ψ_f are near to their rated values.

To prove the noise-tolerant characteristic of TD stated in Section III-C, the simple differential operation ($T_s = 2\ \mu\text{s}$ and $T_d = 2T_s$, the same as TD) expressed in (7) and (12) is also adopted in the experiment, and the results is shown in Fig. 11. It is claimed above that the noise can only be reduced by $1/m$ using simple differential operation, while TD is able to suppress the noise by $1/m^2$, which improves the performance of derivative calculation as well as the subsequent parameter identification. The identification results using simple differential operation are listed in Table VII, from which it is found that larger errors are contained than using TD in the estimation of both inductance and flux linkage.

TABLE VI
(20 °C) SIMULATION RESULTS WITH REDUNDANT METHOD

SIMULATION RESULTS WITH REDUNDANT METHOD						
u_{as}	2/3VDC	1/3VDC	0	-1/3VDC	-2/3VDC	mean rated
amplitude*	119708	121227	120979	120987	119295	- -
offset*	237221	119331	38	-119081	-236856	- -
L (mH)	0.4215	0.4190	-	0.4199	0.4222	0.4207 0.42
ψ_f (Wb)	0.0401	0.0406	0.0405	0.0405	0.0399	0.0403 0.04
EXPERIMENTAL RESULTS WITH REDUNDANT METHOD (ROGOWSKI COIL)						
u_{as}	2/3VDC	1/3VDC	0	-1/3VDC	-2/3VDC	mean rated
amplitude*	91460	102932	100265	105483	100965	- -
offset*	197678	105029	4261	-98114	-197349	- -
L (mH)	0.4912	0.4714	-	0.4640	0.4712	0.4744 0.42
ψ_f (Wb)	0.0349	0.0393	0.0382	0.0402	0.0385	0.0382 0.04
EXPERIMENTAL RESULTS WITH REDUNDANT METHOD (DIFFERENTIAL CIRCUIT)						
u_{as}	2/3VDC	1/3VDC	0	-1/3VDC	-2/3VDC	mean rated
amplitude*	114843	101043	93254	96133	110664	- -
offset*	207395	101014	5041	-93170	-200123	- -
L (mH)	0.4695	0.4949	-	0.4836	0.4630	0.4778 0.42
ψ_f (Wb)	0.0441	0.0388	0.0358	0.0369	0.0425	0.0396 0.04
EXPERIMENTAL RESULTS WITH REDUNDANT METHOD (TD)						
u_{as}	2/3VDC	1/3VDC	0	-1/3VDC	-2/3VDC	mean rated
amplitude*	138944	102903	96739	103910	117557	- -
offset*	235059	99287	-2600	-102287	-222661	- -
L (mH)	0.3997	0.4662	-	0.4765	0.4317	0.4435 0.42
ψ_f (Wb)	0.0495	0.0367	0.0345	0.0370	0.0419	0.0399 0.04

* In the tables (including next), “amplitude” means $\sqrt{B_{aj}^2 + C_{aj}^2}$, “offset” means A_{aj} ($j=1, \dots, 5$) in the a -axis functions (20)-(26).

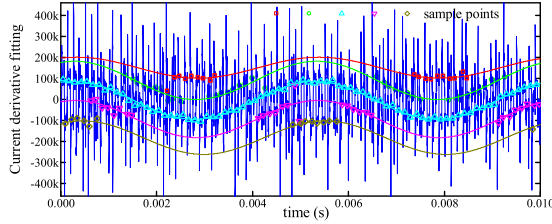


Fig. 11. Worse current derivative fitting results using simple differential operation compared with other methods in Fig. 10(20 °C).

TABLE VII
(20 °C) POOR EXPERIMENTAL RESULTS WITH SIMPLE DIFFERENTIAL OPERATION

u_{as}	2/3VDC	1/3VDC	0	-1/3VDC	-2/3VDC	mean	rated
amplitude	49714	90822	89991	88149	79698	-	-
offset	150982	90431	-4375	-93246	-181406	-	-
L (mH)	0.6115	0.5010	-	0.5345	0.5366	0.5459	0.42
ψ_f (Wb)	0.0218	0.0399	0.0395	0.0387	0.0350	0.0350	0.04

As stated before, this redundant methodology requires, as much as possible, the data of current derivatives in each voltage vector, increasing the complexity of the sampling procedure. Thus, the practical approach is illustrated in Section IV C, with which the sampling of the current derivative will only be conducted in one active vector and one zero vector (in cases like over modulation, sampling might be done in two active vectors as explained before, which will not be discussed any more) during a single PWM period. In the next experimental validations, the differential circuit is the main technique to acquire the current derivative since it can be easily embedded in the inverter system and does not require high-rate ADCs, as well as its low cost, which is summarized in Table II. The

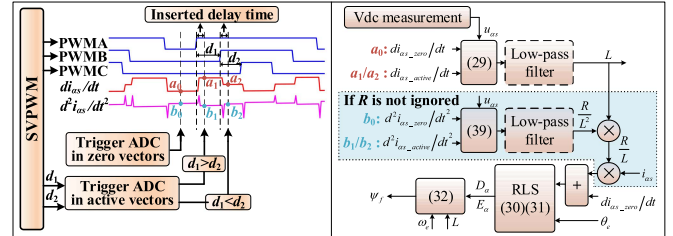


Fig. 12. Overall scheme of implementing the practical approach.

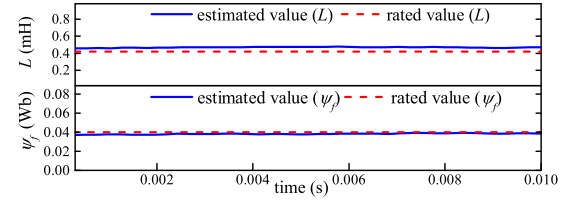


Fig. 13. Experimental results of L and ψ_f using the practical approach with differential circuit (6000 r/min, 20 °C).

overall scheme of implementing the practical approach is shown in Fig. 12, as stated in Section II, the switching state of devices can be monitored through PWM event trigger, e.g., the values of $di_{\alpha s, zero}/dt$ and $d^2 i_{\alpha s, zero}/dt^2$ in zero vectors can be measured by triggering ADC when the up-down count in Fig. 1 comes to zero. Besides, the rising edge of PWMs can also trigger ADC with an inserted delay time to gain $di_{\alpha s, active}/dt$ and $d^2 i_{\alpha s, active}/dt^2$ during active vectors, as explained in Section IV C, the selection of active vector depends on the vector duty cycles (d_1 and d_2) calculated in SVPWM. After the sampling in different vectors, $di_{\alpha s, zero}/dt$ and $di_{\alpha s, active}/dt$ can be used to calculate L through (29) with u_{as} related to the measured Vdc. A low-pass filter might be needed to reject the noises in the differential circuit. If the items of R cannot be ignored, $d^2 i_{\alpha s, zero}/dt^2$ and $d^2 i_{\alpha s, active}/dt^2$ are utilized to figure out R with similar method to estimate L , shown in (39).

Then, subtracting the items of R from $di_{\alpha s, zero}/dt$, the items of flux linkage will be extracted explicitly, as expressed in (28). Using the RLS algorithms in (30) and (31), the magnitude $\sqrt{D_\alpha^2 + E_\alpha^2}$ in (32) could be obtained and finally ψ_f is able to be identified with the previously estimated L and angular speed ω_e . Note that if R can be neglected, $di_{\alpha s, zero}/dt$ can be directly input to the RLS block.

Implementing the practical approach with differential circuit, the experimental results of L and ψ_f at 6000 r/min are enclosed in Fig. 13. Both the identified values of L and ψ_f have an agreement with their rated values. The cumulative errors in the parameter identifications are mainly caused by the parasitic parameters in the circuit as well as in the motor terminal lines, e.g., the line inductance and resistance.

B. DC Bus Voltage Variation

The identification of L depends on the value of u_{as} related to Vdc, as expressed in (3). The variation of Vdc will have an impact on the accurate estimation of L , hence, Vdc should

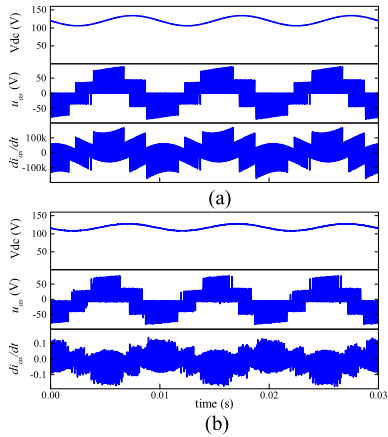


Fig. 14. Waveforms of DC voltage, $u_{\alpha s}$ and $di_{\alpha s}/dt$ (3000 r/min, 20 °C). (a) simulation. (b) experiment.

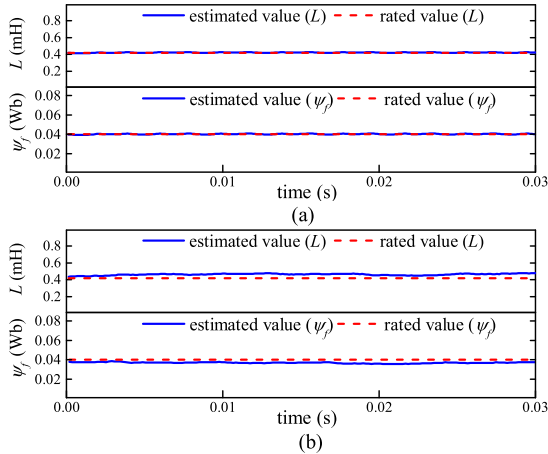


Fig. 15. Parameter identification results of L and ψ_f with V_{dc} variation. (a) simulation. (b) experiment (20 °C).

be measured shown in Fig. 12. To validate the performance of proposed practical approach when the variation of V_{dc} occurs, 100-Hz ripple is injected to the dc voltage (to limit the maximum voltage, the offset dc voltage is reduced to 120 V)

$$V_{dc} = 120 - 10\sqrt{2} \sin(2\pi \times 100t) \quad (\text{V}) . \quad (41)$$

The simulated and experimental waveforms of dc voltage, $u_{\alpha s}$ and $di_{\alpha s}/dt$ (through the differential circuit) at 3000 r/min when the dc voltage variation occurs are shown in Fig. 14. It can be seen that $u_{\alpha s}$ will not be equal to the specific constant values, instead, it is also varying with the variation of dc voltage. Measuring the dc voltage, the values of $u_{\alpha s}$ are able to be corrected, and the estimated parameter results of L and ψ_f in both simulations and experiments are presented in Fig. 15, from which it can be proved that the practical approach is robust to V_{dc} variation.

C. Motor Speed Variation

To evaluate the accuracy of the estimated L and ψ_f with the variation of motor operating speed, the motor decelerates from 6000 to 3000 r/min. The sensitivity of L and ψ_f estimation to

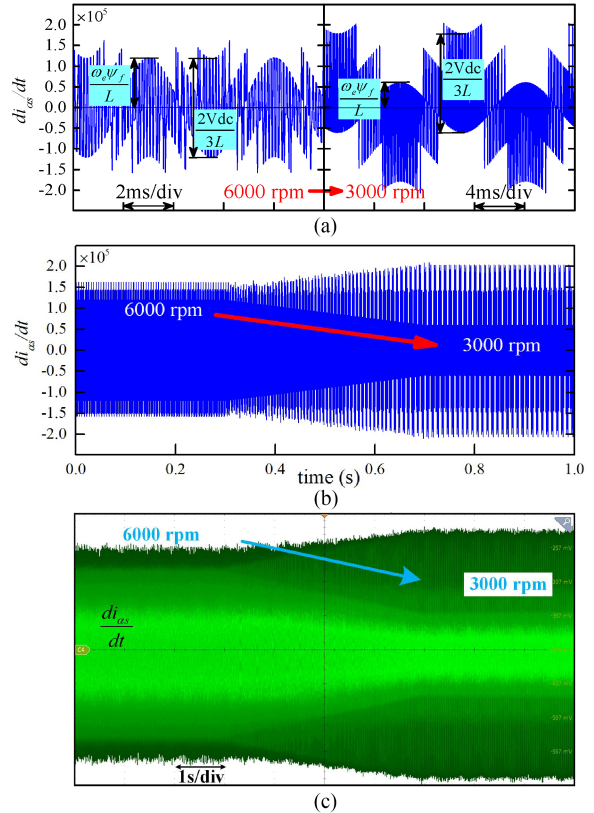


Fig. 16. Waveforms of $di_{\alpha s}/dt$ with speed variation. (a) typical waveforms of current derivative at different speed. (b) simulated overall waveform of $di_{\alpha s}/dt$ (from 6000 to 3000 rpm). (c) experimental overall waveform of $di_{\alpha s}/dt$ (from 6000 to 3000 rpm, 20 °C).

the speed variation is very different. First, it is understood that the estimation of L has nothing to do with the speed, as shown in Fig. 16(a), since the practical approach only requires the value of $u_{\alpha s}$ when identifying L . However, it can be clearly seen from Fig. 16(a) that the estimation of flux linkage is related to the measurement of back EMF, which is extremely sensitive to the operating speed. Thus the operating speed should be accurately measured or estimated when calculating the value of flux linkage, note that the operating speed is also very important in other back EMF-based flux linkage estimation methods.

The overall simulated and experimental waveforms of current derivative when operating speed is from 6000 to 3000 r/min are shown in Fig. 16(b) and (c), respectively. In addition, the simulated and experimental parameter identification results with speed variation are depicted in Fig. 17. From the results, the accuracy of the estimated inductance and flux linkage can still be guaranteed with the variation of operating speed.

D. Low Speed

As explained in Section IV-D, the neglecting of resistance may not be valid in some cases such as low speed, since the proportion of resistance item in the sinusoid part (4) is relatively large. Thus, the value of R could be figured out through the second-order current derivative in (39), and the implementation scheme is given in Fig. 12. The waveforms of $di_{\alpha s}/dt$ and

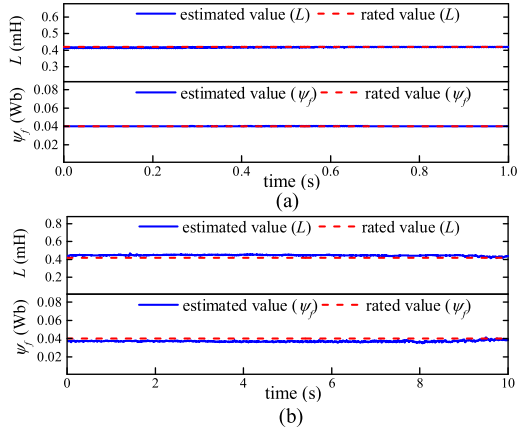


Fig. 17. Identification results of L and ψ_f with speed variation. (a) simulation. (b) experiment (20 °C).

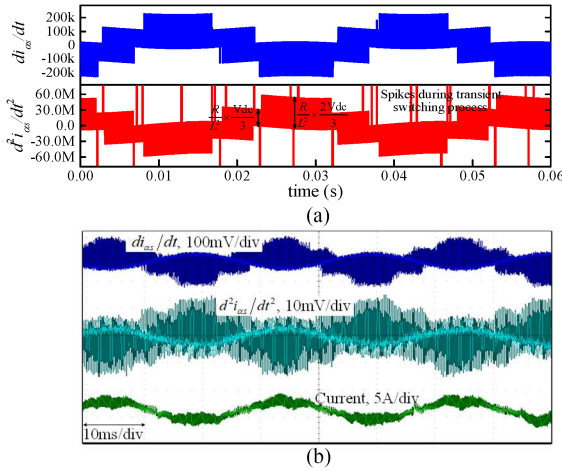


Fig. 18. Waveforms of $di_{\alpha s}/dt$ and $d^2i_{\alpha s}/dt^2$ (1000 r/min, 20 °C). (a) simulation. (b) experiment.

$d^2i_{\alpha s}/dt^2$ in the simulations and experiments when the motor speed is 1000 r/min are presented in Fig. 18. The sampling moment of $d^2i_{\alpha s}/dt^2$ is consistent with $di_{\alpha s}/dt$, as shown in Fig. 12, then according to (39), the information of R can be obtained by

$$R = \left(\frac{d^2i_{\alpha s_zero}}{dt^2} - \frac{d^2i_{\alpha s_active}}{dt^2} \right) \times L^2/u_{\alpha s}. \quad (42)$$

Notice that the value of L has been identified through the first-order current derivative and, obviously, $u_{\alpha s}$ is related to V_{dc} , which means the dc voltage variation will again, influence the accuracy of resistance identification. Besides, it is assumed in (38) that $du_{\alpha s}/dt$ is regarded as zero, however, which is not valid when the dc bus voltage variation occurs. Hence, if considering the V_{dc} variation, dc voltage as well as its derivative should be also measured through, e.g., differential circuit, which will also not be discussed any more in this article. The parameter identification results at 1000 r/min in the simulations and experiments are shown in Fig. 19, from which it is seen that all of the motor parameters including R can be converged to their rated values.

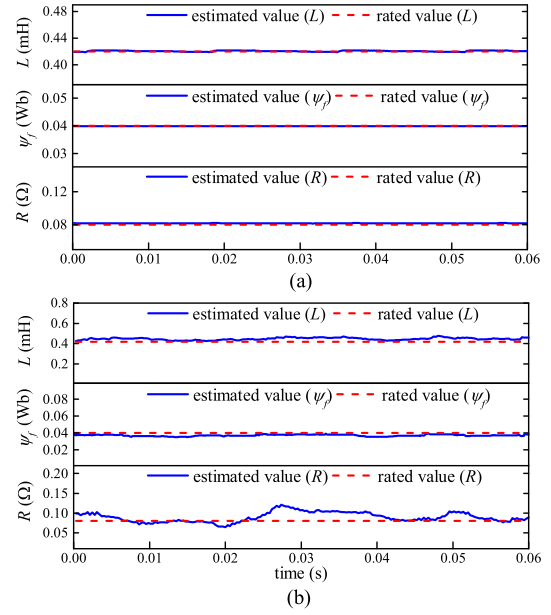


Fig. 19. Parameter identification results (1000 r/min, 20 °C). (a) simulation. (b) experiment.

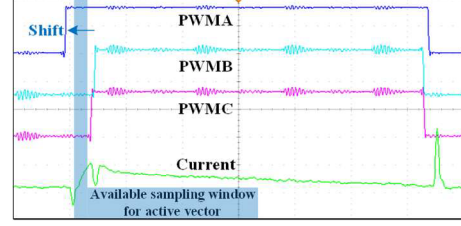


Fig. 20. PWM shift waveform (100 r/min, 20 °C).

Things may become worse at lower speed, e.g., 100 r/min. First, the required voltage is very small at such a low speed (when the load is also slight), causing that the active voltage vectors in SVPWM are very narrow. In this case, technique of PWM shift should be applied, as shown in Fig. 20, an available sampling window can be gained by shifting PWMA to left. The length of shifting is determined by the ADC rate as well as the transient switching time, generally, the duration of several microseconds is enough. Second, the back EMF is extremely small at the speed of 100 r/min, which means it is awfully hard to precisely identify ψ_f with such a small value of back EMF. In other words, the value of ψ_f can be even ignored compared to items of R . The experimental parameter identification results at 100 r/min are given in Fig. 21, L and R are still able to be converged to their rated values but larger errors exist compared with the cases at middle/high speed, while ψ_f cannot be identified accurately, instead, it is nearly zero due to the extremely small back EMF, as analyzed above.

E. Consideration of Parameter Variation

The motor parameters will vary under some conditions. On the one hand, the inductance will deviate primarily with the change of current since the current could influence the magnetic saturation of the iron core [12], however, the installation of permanent

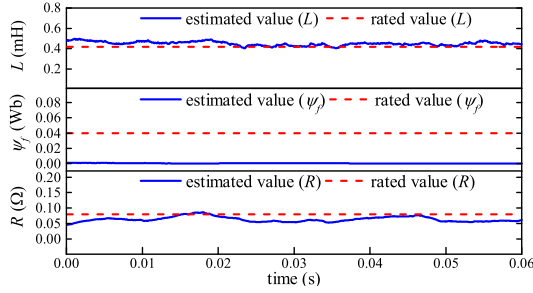


Fig. 21. Experimental parameter identification results (100 r/min, 20 °C).

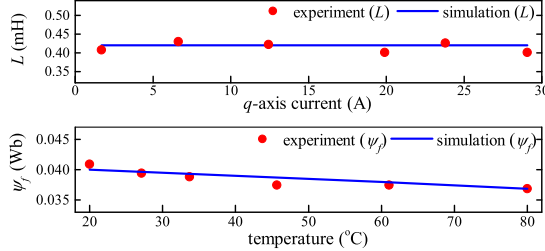


Fig. 22. Experiment and simulation results considering parameter variation (3000 r/min).

magnets on the rotor surface for SPMSMs and large air gap can extend the saturation level, which means the inductance variation is very slight [37]. The FEA-based simulation and experiment results of inductance identification with the change of i_q are given in Fig. 22(top). The motor speed is maintained at 3000 r/min, the values of L when injecting different currents are almost the same according to simulation and their experimental results are adjacent to the simulated ones with minor errors (<5%).

On the other hand, the value of flux linkage is mainly affected by the temperature [12], [19], thus, the FEA-based simulation and experiment results of flux linkage estimation with the increase of temperature are presented in Fig. 22 (bottom). The speed is also 3000 r/min, the flux linkage will decrease with temperature increasing and the experiment results show the agreement with the simulation, the errors are still less than 5%.

F. Performance Comparison With Rotor Position Error

Moreover, to illustrate the merits of the proposed method when rotor position error exists compared with conventional method in $d-q$ rotational coordinate [12], [13], the position error is injected in parameter identification. According to the average model (1), ignoring the items of d -axis current ($i_d = 0$), current derivative and resistance, the parameter identification model is simplified as

$$u_d = -\omega_e L i_q, \quad u_q = \omega_e \Psi_f. \quad (43)$$

The quantities such as $u_{d,q}$ and i_q are from $a-b-c$ coordinate through Park transformation which requires the rotor position angle, thus these quantities will deviate from their real values when rotor position error exists. The same problem occurs when using the average model in $\alpha-\beta$ coordinate (2) since the phases still have an important impact on the parameter identification in such average model [26]. When it comes to the proposed method,

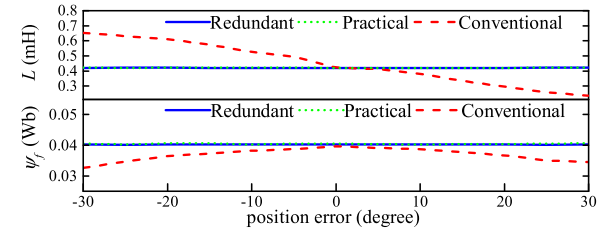
Fig. 23. Identification results of L and ψ_f using different methods with the rotor position error (6000 r/min, 20 °C).

TABLE VIII
COMPARISONS WITH THE CONVENTIONAL METHOD

Method	Proposed practical method	Conventional method
Accuracy	Accurate even with position error	Poor when position error exists
Required sampling	Phase currents, Vdc, speed, current derivatives	Phase currents, Vdc, d/q -axis voltages, speed, rotor position
Computation time	1.81 μ s for executing each iteration of estimation	1.76 μ s for executing each iteration of estimation

considering the rotor position error $\Delta\theta_e$, the switching state function (4) becomes

$$\begin{aligned} \frac{di_{\alpha s}}{dt} &= \frac{u_{\alpha s}}{L} + \frac{\omega_e \Psi_f \sin(\theta_e + \Delta\theta_e)}{L}, \\ \frac{di_{\beta s}}{dt} &= \frac{u_{\beta s}}{L} - \frac{\omega_e \Psi_f \cos(\theta_e + \Delta\theta_e)}{L}. \end{aligned} \quad (44)$$

For one thing, the quantities in $\alpha-\beta$ coordinate such as $u_{\alpha s, \beta s}$ and $i_{\alpha s, \beta s}$ has nothing to do with rotor position, thus rotor position error has no impact on the estimation of L (as well as R). For another, in the proposed method, only the amplitudes of the sinusoid part are taken into account, as seen in (26) and (32), while the phases are not cared, which means the identification of ψ_f is also not affected by rotor position error. The identification results of L and ψ_f using different methods with the rotor position error are demonstrated in Fig. 23, L and ψ_f will deviate from their rated values using the conventional method but will not when using the proposed way in this article, including the redundant and practical methods.

Furthermore, the comparisons with the conventional method in terms of accuracy, required sampling/quantities, and computational time are listed in Table VIII. It should be clearly clarified from the results in Fig. 23 that the accuracy of the proposed method in this article can be guaranteed even with the position errors, while the performance of the conventional method is extremely poor when position error exists. In addition, the proposed practical method will not increase too much computational time (<2 μ s) during the implementation process.

VI. CONCLUSION

An online method to estimate L and ψ_f for inverter-fed SPMSMs using switching state functions is proposed in this article. Based on the dc bus voltage and current derivatives obtained from either hardware or software methods, of which the pros and cons for real-world industrial applications are summarized in

Table III, the clue of identifying L and ψ_f is disclosed. With both the redundant and practical approaches mentioned in this article, L and ψ_f can be finally figured out, which has been validated by simulations and experiments considering the variation of dc voltage, operating speed, and impact of resistance. There are some pronounced advantages in the proposed methods such as avoidance of ill-convergence problems and robustness to rotor position errors. It is also found that there exist difficulties for parameter identification at very low speed (100 r/min), e.g., errors for L/R and no way to identify flux linkage due to very small back EMF, which need further investigations.

REFERENCES

- [1] M. S. Rafaq, F. Mwasilu, J. Kim, H. H. Choi, and J. Jung, "Online parameter identification for model-based sensorless control of interior permanent magnet synchronous machine," *IEEE Trans. Power Electron.*, vol. 32, no. 6, pp. 4631–4643, Jun. 2017.
- [2] Y. Yao, Y. Huang, F. Peng, J. Dong, and H. Zhang, "An improved deadbeat predictive current control with online parameter identification for surface-mounted PMSMs," *IEEE Trans. Ind. Electron.*, vol. 67, no. 12, pp. 10145–10155, Dec. 2020.
- [3] S. Kwak, U. Moon, and J. Park, "Predictive-control-based direct power control with an adaptive parameter identification technique for improved AFE performance," *IEEE Trans. Power Electron.*, vol. 29, no. 11, pp. 6178–6187, Nov. 2014.
- [4] J. Faiz and E. Mazaheri-Tehrani, "Demagnetization modeling and fault diagnosing techniques in permanent magnet machines under stationary and nonstationary conditions: An overview," *IEEE Trans. Ind. Appl.*, vol. 53, no. 3, pp. 2772–2785, May/Jun. 2017.
- [5] IEEE Standard Procedures for Obtaining Synchronous Machine Parameters by Standstill Frequency Response Testing (Supplement to ANSI/IEEE Std 115-1983, IEEE Guide: Test Procedures for Synchronous Machines), IEEE Standard 115A-1987, 1987.
- [6] S. R. P. Reddy and U. Loganathan, "Offline recursive identification of electrical parameters of VSI-fed induction motor drives," *IEEE Trans. Power Electron.*, vol. 35, no. 10, pp. 10711–10719, Oct. 2020.
- [7] S.-H. Lee, A. Yoo, H.-J. Lee, Y.-D. Yoon, and B.-M. Han, "Identification of induction motor parameters at standstill based on integral calculation," *IEEE Trans. Ind. Appl.*, vol. 53, no. 3, pp. 2130–2139, May/Jun. 2017.
- [8] S. A. Odhano, P. Pescetto, H. A. A. Awan, M. Hinkkanen, G. Pellegrino, and R. Bojoi, "Parameter identification and self-commissioning in AC motor drives: A technology status review," *IEEE Trans. Power Electron.*, vol. 34, no. 4, pp. 3603–3614, Apr. 2019.
- [9] M. S. Rafaq and J. Jung, "A comprehensive review of State-of-the-art parameter estimation techniques for permanent magnet synchronous motors in wide speed range," *IEEE Trans. Ind. Informat.*, vol. 16, no. 7, pp. 4747–4758, Jul. 2020.
- [10] Y. Inoue, Y. Kawaguchi, S. Morimoto, and M. Sanada, "Performance improvement of sensorless IPMSM drives in a low-speed region using online parameter identification," *IEEE Trans. Ind. Appl.*, vol. 47, no. 2, pp. 798–804, Mar./Apr. 2011.
- [11] Y. Yao, Y. Huang, F. Peng, and J. Dong, "Position sensorless drive and online parameter estimation for surface-mounted PMSMs based on adaptive full-state feedback control," *IEEE Trans. Power Electron.*, vol. 35, no. 7, pp. 7341–7355, Jul. 2020.
- [12] S. J. Underwood and I. Husain, "Online parameter estimation and adaptive control of permanent-magnet synchronous machines," *IEEE Trans. Ind. Electron.*, vol. 57, no. 7, pp. 2435–2443, Jul. 2010.
- [13] D. Q. Dang, M. S. Rafaq, H. H. Choi, and J. Jung, "Online parameter estimation technique for adaptive control applications of interior PM synchronous motor drives," *IEEE Trans. Ind. Electron.*, vol. 63, no. 3, pp. 1438–1449, Mar. 2016.
- [14] P. Vaclavek, P. Blaha, and I. Herman, "AC drive observability analysis," *IEEE Trans. Ind. Electron.*, vol. 60, no. 8, pp. 3047–3059, Aug. 2013.
- [15] T. Boileau, N. Leboeuf, B. Nahid-Mobarakeh, and F. Meibody-Tabar, "Online identification of PMSM parameters: Parameter identifiability and estimator comparative study," *IEEE Trans. Ind. Appl.*, vol. 47, no. 4, pp. 1944–1957, Jul./Aug. 2011.
- [16] A. T. Nguyen, V. N. Nguyen, and D.-C. Lee, "Parameter identification of inverter-fed induction machines at standstill based on signal injection," in *Proc. IEEE Energy Convers. Congr. Expo.*, 2021, pp. 4902–4907.
- [17] G. Feng, C. Lai, K. Mukherjee, and N. C. Kar, "Online PMSM magnet flux-linkage estimation for rotor magnet condition monitoring using measured speed harmonics," *IEEE Trans. Ind. Appl.*, vol. 53, no. 3, pp. 2786–2794, May/Jun. 2017.
- [18] G. Feng, C. Lai, and N. C. Kar, "Particle-filter-based magnet flux linkage estimation for PMSM magnet condition monitoring using harmonics in machine speed," *IEEE Trans. Ind. Informat.*, vol. 13, no. 3, pp. 1280–1290, Jun. 2017.
- [19] N. Z. Popov, S. N. Vukosavic, and E. Levi, "Motor temperature monitoring based on impedance estimation at PWM frequencies," *IEEE Trans. Energy Convers.*, vol. 29, no. 1, pp. 215–223, Mar. 2014.
- [20] R. Raja, T. Sebastian, and M. Wang, "Online stator inductance estimation for permanent magnet motors using PWM excitation," *IEEE Trans. Transp. Electrific.*, vol. 5, no. 1, pp. 107–117, Mar. 2019.
- [21] K. Choi, Y. Kim, K.-S. Kim, and S.-K. Kim, "Using the stator current ripple model for real-time estimation of full parameters of a permanent magnet synchronous motor," *IEEE Access*, vol. 7, pp. 33369–33379, 2019.
- [22] Z. Mynar, P. Vaclavek, and P. Blaha, "Synchronous reluctance motor parameter and state estimation using extended Kalman filter and current derivative measurement," *IEEE Trans. Ind. Electron.*, vol. 68, no. 3, pp. 1972–1981, Mar. 2021.
- [23] S. Xiao and A. Griffio, "PWM-based flux linkage and rotor temperature estimations for permanent magnet synchronous machines," *IEEE Trans. Power Electron.*, vol. 35, no. 6, pp. 6061–6069, Jun. 2020.
- [24] J. Zhang, F. Peng, Y. Huang, Y. Yao, and Z. Zhu, "Online inductance identification using PWM current ripple for position sensorless drive of high-speed SPMSM," *IEEE Trans. Ind. Electron.*, vol. 69, no. 12, pp. 12426–12436, Dec. 2021.
- [25] M. X. Bui, M. Faz Rahman, D. Guan, and D. Xiao, "A new and fast method for on-line estimation of d and q axes inductances of interior permanent magnet synchronous machines using measurements of current derivatives and inverter DC-bus voltage," *IEEE Trans. Ind. Electron.*, vol. 66, no. 10, pp. 7488–7497, Oct. 2019.
- [26] Y. Yu et al., "Full parameter estimation for permanent magnet synchronous motors," *IEEE Trans. Ind. Electron.*, vol. 69, no. 5, pp. 4376–4386, May 2022.
- [27] Texas Instruments Incorporated, "TMS320F2837xD dual-core delfino microcontrollers technical reference manual (Rev. I)," Sep. 2019. [Online]. Available: https://www.ti.com/lit/ug/spruhm8i/spruhm8i.pdf?ts=1647485135386&ref_url=https%253A%252F%252Fwww.ti.com%252Fproduct%252FTMS320F2837D
- [28] R. Arablouei, K. Doğançay, and T. Adalı, "Unbiased recursive least-squares estimation utilizing dichotomous coordinate-descent iterations," *IEEE Trans. Signal Process.*, vol. 62, no. 11, pp. 2973–2983, Jun. 2014.
- [29] A. Mingotti, L. Peretto, and R. Tinarelli, "A smart frequency domain-based modeling procedure of Rogowski coil for power systems applications," *IEEE Trans. Instrum. Meas.*, vol. 69, no. 9, pp. 6748–6755, Sep. 2020.
- [30] B.-Z. Guo and J.-Q. Han, "A linear tracking-differentiator and application to the online estimation of the frequency of a sinusoidal signal," in *Proc. IEEE Int. Conf. Control Appl.*, 2000, pp. 9–13, doi: 10.1109/CCA.2000.897391.
- [31] J. Han, "From PID to active disturbance rejection control," *IEEE Trans. Ind. Electron.*, vol. 56, no. 3, pp. 900–906, Mar. 2009.
- [32] Y. Gu, F. Ni, D. Yang, and H. Liu, "Switching-state phase shift method for three-phase-current reconstruction with a single DC-link current sensor," *IEEE Trans. Ind. Electron.*, vol. 58, no. 11, pp. 5186–5194, Nov. 2011.
- [33] J. Ha, "Voltage injection method for three-phase current reconstruction in PWM inverters using a single sensor," *IEEE Trans. Power Electron.*, vol. 24, no. 3, pp. 767–775, Mar. 2009.
- [34] J. Holtz, W. Lotzkat, and A. M. Khambadkone, "On continuous control of PWM inverters in the overmodulation range including the six-step mode," *IEEE Trans. Power Electron.*, vol. 8, no. 4, pp. 546–553, Oct. 1993.
- [35] S. Bolognani and M. Zigliotto, "Novel digital continuous control of SVM inverters in the overmodulation range," *IEEE Trans. Ind. Appl.*, vol. 33, no. 2, pp. 525–530, Mar./Apr. 1997.
- [36] A. M. Hava, R. J. Kerkman, and T. A. Lipo, "Carrier-based PWM-VSI overmodulation strategies: Analysis, comparison, and design," *IEEE Trans. Power Electron.*, vol. 13, no. 4, pp. 674–689, Jul. 1998.
- [37] M. Zafarani, T. Goktas, B. Akin, and S. E. Fedigan, "An investigation of motor topology impacts on magnet defect fault signatures," *IEEE Trans. Ind. Electron.*, vol. 64, no. 1, pp. 32–42, Jan. 2017.



Xiaoyan Huang (Member, IEEE) received the B.E. degree in control measurement techniques and instrumentation from Zhejiang University, Hangzhou, China, in 2003, and the Ph.D. degree in electrical machines and drives from the University of Nottingham, Nottingham, U.K., in 2008.

From 2008 to 2009, she was a Research Fellow with the University of Nottingham. Currently, she is a Professor with the College of Electrical Engineering, Zhejiang University, where she is working on electrical machines and drives. Her research interests include PM machines and drives for aerospace and traction applications, and generator system for urban networks.



Yelong Yu was born in Zhejiang, China, in 1995. He received the B.Eng. degree in 2018 from Zhejiang University, Hangzhou, China, where he is currently working toward the Ph.D. degree, both in electrical engineering.

His research interests include the motor drive and control for permanent magnet synchronous motors.



Zhaokai Li was born in Lishui, China, in 1993. He received the B.S. and Ph.D. degrees in electrical engineering from Zhejiang University, Hangzhou, China, in 2015 and 2020, respectively.

He is currently a Postdoctoral Researcher with Zhejiang University. His major research interests include the analytical modelling of PMSM and iron loss analysis.



Zhuo Chen was born in Sichuan Province, China, in 1996. He received the B.S. in electrical engineering in 2018 from Zhejiang University, Hangzhou, China, where he is currently working toward the Ph.D. degree in electrical machines and drives.

His current research interest includes the design of permanent-magnet machines for aerospace and traction applications.



Shaopo Huang received the B.S., M.S., and Ph.D. degrees in electrical engineering from the Hebei University of Technology, Tianjin, China, in 2009, 2012, and 2021, respectively.

He was an Engineer with ABB LV Installation Materials Company, Ltd., Beijing, China, from 2012 to 2015. From 2017 to 2019, he was a Research Fellow with Electrical Machines and Drives Laboratory, Michigan State University, East Lansing, MI, USA. He is currently with the College of Information Technology, Beijing Institute of Petrochemical Technology, Beijing, China. His research interests include fault diagnosis and mitigation of electrical machines and drives, and reliability testing of electrical apparatus.



Feng Niu (Member, IEEE) was born in Hebei, China, in 1986. He received the B.S. and Ph.D. degrees in electrical engineering from the Hebei University of Technology, Tianjin, China, in 2009 and 2015, respectively.

From 2012 to 2014, he was a Research Fellow with Electrical Machines and Drives Laboratory, Michigan State University, East Lansing, MI, USA. From 2016 to 2018, he was a Postdoctoral Research Fellow with the College of Electrical Engineering, Zhejiang University, Hangzhou, China. He is currently a Professor with the School of Electrical Engineering, Hebei University of Technology. He has authored or coauthored more than 50 technical articles. His current research interests include motor system and control, and intelligent electrical equipment.



Jian Zhang received the Ph.D. degree in mechanical engineering from Zhejiang University, Hangzhou, China, in 2010.

He is currently an Associate Professor of Electrical Engineering with Zhejiang University. His current research interests include design, control, and reliability analysis of electrical machines.